Potential dependence of the bifurcation structure in generalized Duffing oscillators

Ching Sheu Wang*
Institute of Electro-Optical Engineering, National Chiao-Tung University, 1001 Ta Hsueh Road, Hsinchu, Taiwan 30050, Republic of China

Yao Huang Kao
Department of Communication Engineering, National Chiao-Tung University, 1001 Ta Hsueh Road, Hsinchu, Taiwan 30050, Republic of China

Jeun Chyuan Huang
Communication Technology Division, Industrial Technology Research Institute, Chung Chen Road, Hsinchu, Taiwan 30050, Republic of China

Yih Shun Gou
Institute of Electrophysics, National Chiao-Tung University, 1001 Ta Hsueh Road, Hsinchu, Taiwan 30050, Republic of China
(Received 5 August 1991)

The features of various bifurcations in forced Duffing oscillators are extensively investigated by means of numerical simulation. Some common features in four types of potential well are found. With reference to the transition boundaries in parameter space, the influences of local symmetry properties of the potential well on the bifurcation routes are indicated and definite functional forms of the border line in ω-k space separating the region with simple stable period-1 solutions from the region with complicated solutions are determined. A method combining Floquet theory with harmonic balance is presented to describe the mechanism of the transitions.

PACS number(s): 64.60.Cn, 64.10.+h

I. INTRODUCTION

Since the discovery of the Lorenz attractor [1] in 1963, a number of researchers have paid much attention to finding the global features of chaos and routes to chaos. Indeed, owing to the great efforts in theoretical and experimental work, enormous progress has currently been made in this field [2–4]. The most important finding in this subject is that the routes to chaos in nonlinear dynamical systems exhibit a universal manner and can be characterized by several scaling constants; this is reminiscent of the situation in phase transitions [5,6]. So far, three scenarios of routes to chaos have been mentioned. They are the Feigenbaum [7], intermittency [8], and quasiperiodic routes [9], and are related to the period-doubling (PD) bifurcation, saddle-node (SN) bifurcation, and Hopf bifurcation, respectively [10,11].

Basically, from the view point of local bifurcations the PD can be classified into two types. One is supercritical and the other is subcritical. Both occur with one of the eigenvalues crossing the unit circle at -1. In the former case, there is an exchange of stability from one stable state to the other stable states. The latter has no exchange of stability; instead, stability is lost locally at the bifurcation point [10,11]. The intermittent routes are also classified into three types [10,11]. For type-I intermittency it is associated with SN bifurcation and the stable state becomes unstable with the dominant eigenvalue passing through $+1$. For type-II intermittency it is associated with the subcritical Hopf bifurcation; two eigenvalues cross the unit circle in the complex plane. And for type-III intermittency it is associated with a subcritical PD bifurcation; the dominant eigenvalue passes through -1. However, in practical physical systems, these bifurcations often tangle with each other in a complicated manner. The dynamics of transition of such systems has been extensively studied along the line of these scenarios by many authors [12–15].

Among these systems, the forced Duffing oscillator governed by the equation

$$\ddot{x}+k\dot{x}+\frac{dV(x)}{dx}=F\sin(\omega t) \tag{1}$$

is one of the most important systems to elucidate the chaotic dynamics, where $V(x)$ is an anharmonic potential function, k is the phenomenological damping factor, F is the driving amplitude, ω is the driving frequency, and the overdot denotes the derivative with respect to time t. This equation has been utilized to model a wide variety of physical systems such as the optical bistability in the multiple-photon absorption process, soft and hard springs, buckled beam, four-wave interaction, and plasma oscillation [12–15], etc. In general, the potential function $V(x)$ is described by

$$V(x)=\frac{\alpha}{2}x^2+\frac{\beta}{3}x^3+\frac{\gamma}{4}x^4 ,$$

with α, β, and γ coefficients. By means of some transformations [16], either β or γ can be set to zero. Actually, it embraces four types of potential. The potential

$$V_1=\frac{\alpha}{2}x^2+\frac{\beta}{3}x^3$$

with $\alpha>0$ and $\beta<0$ has one minimum at $x=0$ and one maximum at $x=-\alpha/\beta$ and is asymmetrical with respect to the minimum point as shown in Fig. 1(a). The swing is around the minimum and the potential increases through the unbounded side with $x>1-\alpha/\beta$. For potential

$$V_2=\frac{\alpha}{2}x^2+\frac{\gamma}{4}x^4,$$

with $\alpha<0$ and $\gamma>0$, there are two wells which are locally asymmetrical with respect to two minima at $x=\pm\sqrt{-\alpha/\gamma}$ and globally symmetrical with respect to $x=0$, as shown in Fig. 1(b). The swing exists either in one local well or among the two wells. For potential

$$V_3=\frac{\alpha}{2}x^2+\frac{\gamma}{4}x^4,$$

with $\alpha>0$ and $\gamma<0$, the well has one minimum at $x=0$ and two maxima at $x=\pm\sqrt{-\alpha/\gamma}$ and is symmetrical with respect to $x=0$, as shown in Fig. 1(c). The motion is confined between two maxima and may escape with $|x|$ larger than $\sqrt{-\alpha/\gamma}$. For potential

$$V_4=\frac{\alpha}{2}x^2+\frac{\gamma}{4}x^4,$$

with $\alpha>0$ and $\gamma>0$, the well is bounded and is symmetrical with respect to a minimum at $x=0$, as shown in Fig. 1(d). The swing is always confined within the well. Of the four potentials reviewed above, all except V_4 contain inflection points.

Some dynamic implications of Eq. (1) are well known. For example, its stable periodic solutions encompass many phenomena, including primary and secondary resonances, and a multiattractor with hysteresis [17], whereas for the chaotic solutions some exotic features have been presented, such as Feigenbaum routes to chaos, attractors hopping with $1/f$ noise [15], crises of attractors [18,19], and homoclinic chaos [14] etc. In fact, all of the studies related to Eq. (1), so far, in either experimental or theoretical work, are truly fragmentary [13,20–22]; a systematic understanding of the dynamics covering the whole range of parameters is yet to be found. Consequently, more information concerning the physical features, either in bifurcations or in chaos, is still to be obtained. To this end, we will focus on studying the bifurcation structure in various types of potential well and pay special attention to the role of the symmetry property of the well on the bifurcation route to chaos. The interrelationships of controlled parameters with the occurrence of various bifurcations, including crisis, intermittency, hysteresis and PD bifurcation, are especially considered. We also note that the border line separating the complicated solution region from the simple stable period-1 solution region in ω and k parameter space is presented in terms of a simple function. In fact, we hope that this study allows us to give a certain kind of global

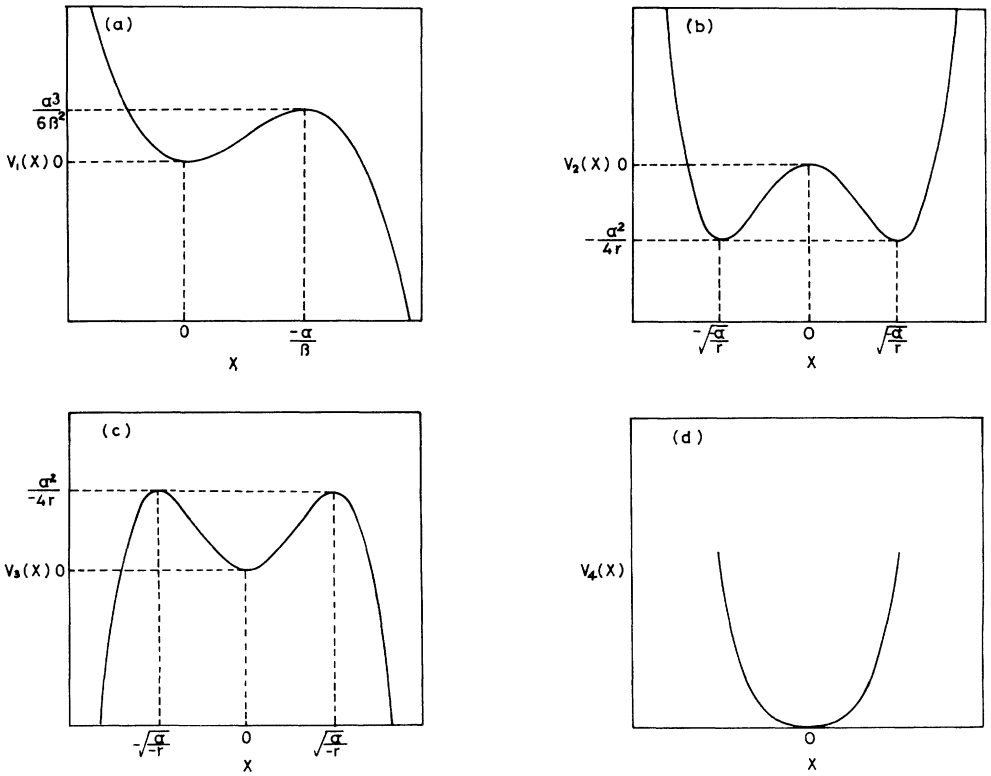

FIG. 1. The potentials V as a function of x. (a) Asymmetrical one-well potential; $V_1(x)=(\alpha/2x^2+(\beta/3)x^3$ where $\alpha>0$ and $\beta<0$. (b) Two-well potential; $V_2(x)=(\alpha/2)x^2+(\gamma/4)x^4$ where $\alpha<0$ and $\gamma>0$. (c) Symmetrical one-well potential; $V_3(x)=(\alpha/2)x^2+(\gamma/4)x^4$ where $\alpha>0$ and $\gamma<0$. (d) Infinitely bounded symmetrical one-well potential; $V_4(x)=(\alpha/2)x^2+(\gamma/4)x^4$ where $\alpha>0$ and $\gamma>0$.

picture about the dynamic transition in the Duffing oscillator, and to act as a guide for uncovering the dynamical behavior in real experiments. A method combining Floquet theory and harmonic balance is applied to interpret the observations and thus to obtain an understanding of the predominant mechanism of the various kinds of transitions.

The paper is organized as follows. Section II describes the method and the observations in the numerical experiment. Section III provides a mathematical way to systematically analyze the above results. Finally, conclusions are given in Sec. IV.

II. NUMERICAL EXPERIMENT

From previous work [18–21,23], we know that as regards to various potentials Eq. (1) can be reduced to the simpler forms which are shown in Table I. Only three controlled parameters (k, ω, and F) need be considered in tracing the transitions. Because the equations cannot be solved exactly, here, numerical computation with the fourth-order Runge-Kutta algorithm is employed. The transitions are characterized by tracing the time evolution, phase portrait $(x(t),\dot{x}(t))$ and the Fourier spectrum. Besides that, for the periodically forced oscillators as in our cases, the transitions can be identified from the stroboscopically sampled data $(x(n),\dot{x}(n))$ at $t=2n\pi/\omega$, where n is an integer. This has been done. This reduced two-dimensional set is referred to as a Poincaré section and a corresponding map $P_\Sigma(x(n),\dot{x}(n)) \rightarrow (x(n+1),\dot{x}(n+2))$ is called a Poincaré map. Let us assume that $P_\Sigma(X^*)=P_\Sigma(x^*,\dot{x}^*)=X^*$, then $X^*=(x^*,\dot{x}^*)$ is a fixed point of P_Σ. The fixed point in the Poincaré section is just equivalent to the limit cycle in the phase space. Hence the transitions of limit cycle can be inferred from the variations of the corresponding fixed point, while an effective method of tracing the fixed point may be nontrivial. Here, a method based on the Newton-Raphson algorithm is used to trace out quickly both the stable and unstable fixed points [24]. If $P_\Sigma(x,\dot{x})$ is smooth, then the fixed point X^* can be calculated by iterating from an initial guess $x^{(0)}$ using the relation

$$X^{(i+1)}=X^{(i)}-DH(X^{(i)})^{-1}H(X^{(i)}) , \tag{2}$$

where $H(X^*)=X^*-P_\Sigma(X^*)=0$ and the superscript (i) indicates the iteration count. From the eigenvalue of the Jacobian of fixed points, $DP_\Sigma(X^*)$, not only the criterion of the stability of the fixed point can be determined but also the type of the local bifurcation.

In order to get as much information as possible, two scanning procedures, by varying ω at a fixed F (frequency scanning) and by varying F at a fixed ω (amplitude scanning), are made with k as a parameter. Consequently, all the thresholds of possible transitions in terms of controlled parameters can be obtained experimentally in the state diagram [18–21,23]. Some salient results are presented in the following.

A. For the case of V_1 potential ($\alpha=1$ and $\beta=-1$)

The state diagram is shown in Fig. 2(a). The transition boundaries include hysteresis (dashed line), PD (solid line), crisis (short-dashed–long-dashed), and intermittency (dotted line). The shape of the transition boundaries looks like a swallow tail in each resonant region. The typical bifurcation diagrams obtained with the method of amplitude scanning at fixed frequencies $\omega=0.48$, 0.54, 0.86, 1.1, 1.8, and 2.1 are detailed in Fig. 2(b). In the primary resonant region (marked A_1), right after the hysteresis loop, the Feigenbaum route is observed with excitation frequency at the right-hand side of the interception point of the hysteresis boundary and crisis boundary with $\omega_{CA}=0.812$. When the excitation frequency is set at the left-hand side of ω_{CA}, due to the hysteresis induced crisis and intermittency, two kinds of basins are exhibited in the system. One either follows the type-I intermittency route to chaos or escapes the well. The other follows the Feigenbaum route to chaos in which the chaotic attractor finally is to be destroyed by the crisis as the driving amplitude is increased further. In the secondary resonant region (marked B_1), the transitions are more complicated. For $\omega_{CB}<\omega<\omega_{SB}$, the first PD is subcritical, where the PD and hysteresis jump occur simultaneously. At the onset point of subcritical PD the eigenvalue is proven to be equal to -1. Subsequently the route of the subcritical case follows the Feigenbaum scenario. For $\omega<\omega_{CB}$, the observed solution follows the type-III intermittency with the eigenvalue also crossing -1 and then escapes through the unbounded side. The second return map, $x(n+2)$ versus $x(n)$, with frequency $\omega=1.74$ and $F=0.459$ is shown to demonstrate this situation in Fig. 2(c). We note that the occurrence of subcritical PD and type-III intermittency is due to the asymmetrical potential of the system. The same as in the primary resonant region, the strange attractor destroyed by the boundary crises can also be discovered in this region ($\omega<\omega_{CB}$) by the proper initial conditions (or by the method of fixed excitation force and scanning frequency). Furthermore,

TABLE I. Reduced forms of Eq. (1) used in this work.

$\ddot{x}+k\dot{x}+\lvert\alpha\rvert x-\lvert\beta\rvert x^2=F\sin\omega t$	$\omega_0=\sqrt{\lvert\alpha\rvert}$, $c=\lvert\alpha\beta\rvert$, $k_1=k/\omega_0$, $\Omega=\omega/\omega_0$, $F_1=F/\lvert\alpha c\rvert$	$\ddot{z}+k_1\dot{z}+z+z^2=F_1\sin(\Omega\tau)$
$\ddot{x}+k\dot{x}+\lvert\alpha\rvert x-\lvert\gamma\rvert x^3=F\sin\omega t$	$\omega_0=\sqrt{\lvert\alpha\rvert}$, $c=\omega_0/\sqrt{\lvert\gamma\rvert}$, $k_1=k/\omega$, $\Omega=\omega/\omega_0$, $F_1=F/\lvert\alpha c\rvert$	$\ddot{z}+k_1\dot{z}+z-z^3=F_1\sin(\Omega\tau)$
$\ddot{x}+k\dot{x}\pm\lvert\alpha\rvert x-\lvert\gamma\rvert x^3=F\sin\omega t$	$\omega_0=\sqrt{\lvert\alpha\rvert}$, $c=\omega_0/\sqrt{\lvert\gamma\rvert}$, $k_1=k/\omega_0$, $\Omega=\omega/\omega_0$, $F_1=F/\lvert\alpha c\rvert$	$\ddot{z}+k_1\dot{z}\pm z+z^3=F_1\sin(\Omega\tau)$

as $\omega > \omega_{SB}$, the first PD is supercritical.

In the estate diagram, we note that the curve of PD folds back (i.e., the transition boundary of the last reverse PD) at a frequency near $\omega \cong 2$. The complicated solutions exist only with the parameters inside the shaded region as shown in the inset of Fig. 2(a). According to our experiments, it is worth mentioning that the folding frequency ω_F, corresponding to the folding point, is found to be a function of the damping factor k with a simple form,

$$\omega_F(k)=\omega_0 \operatorname{sech}^2\left[\frac{k}{k_0}\right], \tag{3}$$

where the constants $\omega_0=2.215$ and $k_0=1.78$; see Fig. 2(d). This equation can be used to determine whether a complicated or simple solution can be applied in this nonlinear system.

B. For the case o potential V_2 ($\alpha=-1$ and $\gamma=1$)

The state diagram is shown in Fig. 3(a). As regards the motion in one of the local wells, the shape of the transition boundaries also looks like a swallow tail. The supercritical PD and type-I intermittency are observed at the primary resonant region (marked A_1). And the subcritical PD bifurcation and type-III intermittency are found at the secondary resonant region (marked B_1). These situations are similar to the previous case. The bifurcation diagrams are shown in Figs. 3(b)–3(g). After the occurrence of intermittency or Feigenbaum route to chaos, the motion will hop between the two valleys. With further increasing the excitation amplitude up to curve H_u, the solution becomes stable with the swing throughout two valleys. In this situation the dynamics of the swing closely resembles the case of the infinitely bounded poten-

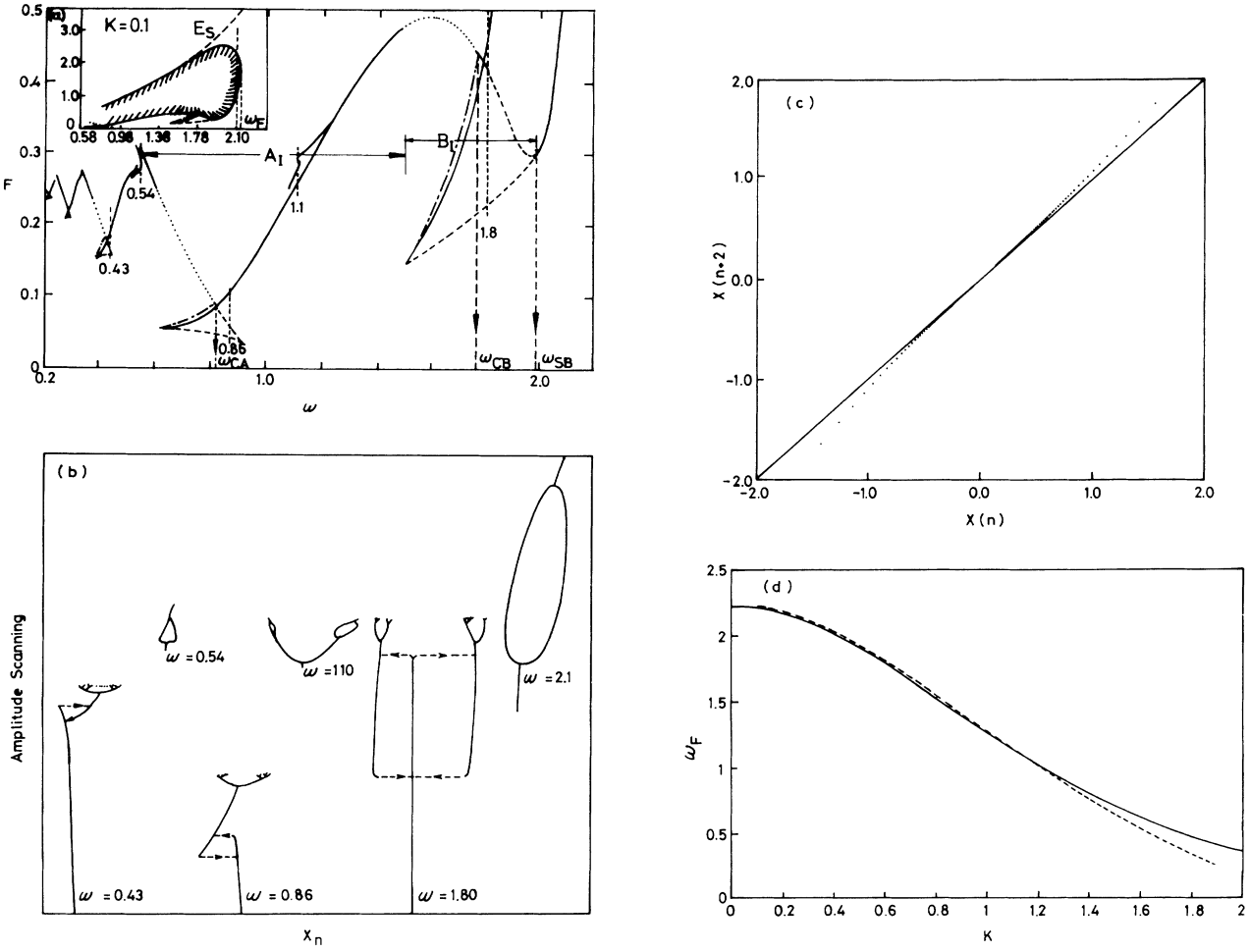

FIG. 2. (a) The state diagram for the asymmetrical one-well potential with controlled parameters $k=0.1$, $\alpha=1$, and $\beta=-1$. Regions A_1 and B_1 correspond to the primary and subharmonic resonance, respectively. The solid line (——) denotes the threshold of period doubling, the dashed line (— — —) denotes the threshold of hysteresis jump, the dotted line (· · · ·) denotes the threshold of intermittency, and the short-dashed–long-dashed (—·—·) denotes the threshold of crises event. The curve E_s represents the border line of escaping the potential well. (b) Bifurcation diagrams for amplitude F scanning with driven frequencies $\omega=0.43$, 0.54, 0.86, 1.10, 1.80, and 2.1. (c) The second return map with frequency $\omega=1.74$ and $F=0.459$. (d) The folding frequency ω_F as a function of the damping factor k, where the solid line is from Eq. (3) and the dashed line is from the experimental results.

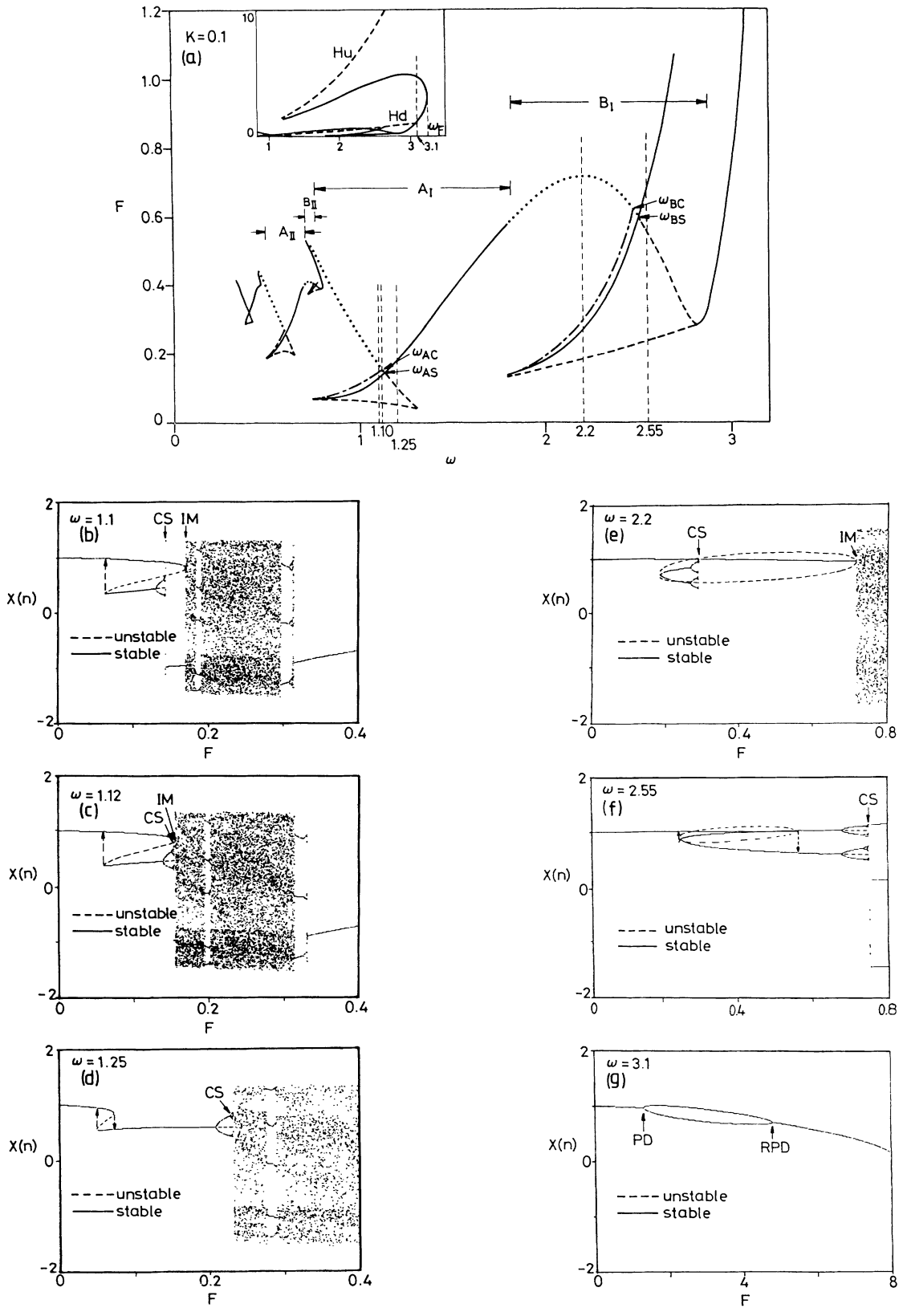

FIG. 3. (a)The state diagram for the two-well potential with controlled parameters $k=0.1$, $\alpha=-1$, and $\gamma=1$. Regions A_I and B_I correspond to the primary and subharmonic resonance, respectively. The solid line (——) denotes the threshold of period doubling, the dashed line (— — —) denotes the threshold of hysteresis jump, the dotted line (· · · ·) denotes the threshold of intermittency, and the short-dashed–long-dashed line (—·—·) denotes the threshold of crises event. Bifurcation diagram in amplitude scanning with driven frequency at (b) $\omega=1.1$,(c) $\omega=1.12$ for (d) $\omega=1.25$, (e) $\omega=2.20$, (f) $\omega=2.55$, and (g) $\omega=3.1$.

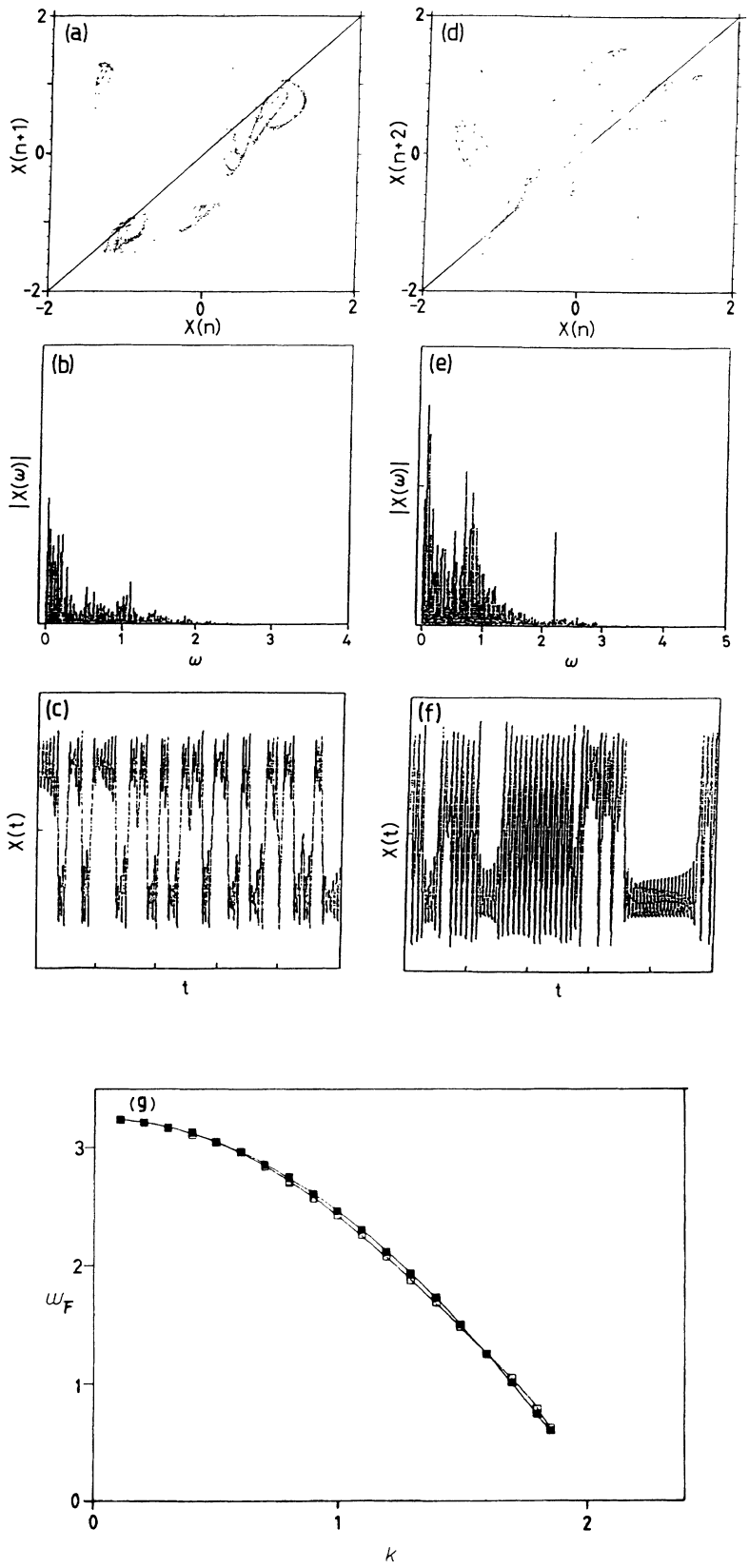

FIG. 4. (a) Return map, (b) Fourier spectrum, and (c) Time evolution for $\omega=1.1$ and $F=0.171$. (d) Second return map, (e) Fourier spectrum, and (f) Time evolution for $\omega=2.20$ and $F=0.714$. (g) The folding frequency ω_F as a function of the damping k, where □ denotes the experimental results and ■ denotes the results fitted by Eq. (4).

tial (V_4), while the small effect of the bump in the well is negligible.

Since the observation of the relationship between the low-frequency noise ($1/f$) and the hopping phenomena in nonlinear dynamics [13–15], the subject has been of current interest. In the primary resonant region with $\omega < 1.14$ the hopping starts right after the occurrence of intermittency and results in a low-frequency noise. This is illustrated by the typical case with $\omega = 1.1$, as shown in Figs. 4(a)–4(c) depicting the return map, Fourier spectrum, and time evolution, respectively. These are classified as intermittency-induced hopping [19]. While $\omega > 1.14$ the hopping begins via the effect of the crisis preceded by a Feigenbaum route and also produces the low-frequency noise with $1/f$ shape in the spectrum [18]. But for $\omega < 1.14$, in which case the boundary crisis interrupts the hysteresis structure, the strange attractor of one of the branches of the hysteresis loop suddenly disappears, and the hopping phenomenon does not appear. In order to further compare the basic nature of the type-I and type-III intermittency-induced hopping the return maps, Fourier spectrum, and time evaluations with frequency $\omega = 2.2$ are shown in Figs. 4(d)–4(f), respectively. For both types the time evolution is equally likely to be in either valley and gives rise to the low-frequency noise. For type-III intermittency, the eigenvalue precisely crosses -1, and the time evolution contains a subharmonic with growing amplitude, and a fundamental with decaying amplitude in the laminar region, and has a strong component with frequency near half of the excitation one. The second return map, $x(n+2)$ versus $x(n)$, as shown in Fig. 4(d), provides a further means to differentiate type-III intermittency from type-I. In type-III intermittency two dense sets cross the diagonal of the second return map; while for type-I intermittency, the two dense sets are just tangent to the diagonal of the first return map. This is an essential difference between type-III and type-I. It is evident that the essential mechanism of the occurrence of the $1/f$ noise in both cases comes from the hopping between the two attractors.

In the state diagram, Fig. 3(a), the curves of period doubling are also folded. The folding frequency ω_F is found to be dependent on the damping factor k. And this relation can be fitted to satisfy the following equation:

$$\omega_F(k) = \omega_0 \left[1 - \left(\frac{k}{k_0} \right)^2 \right] , \tag{4}$$

where the constants $\omega_0 = 3.247$ and $k_0 = 2.045$; see Fig. 4(g). If the driving frequency is beyond the folding frequency $\omega_F(k)$ and the driving force amplitude does not exceed the boundary H_u, the complicated solution cannot occur. A similar result has also been discovered in the case with a sinusoidal period potential well but with $\omega_0 = 1.473$ and $k_0 = 1.656$. Equation (4) provides a crucial condition to determine whether the solution is simple or complicated.

C. For the case of V_3 potential ($\alpha = 1$ and $\gamma = -1$)

The state diagram for the transition boundaries with swallow-tailed form is shown in Fig. 5(a) with damping factor $k = 0.1$, driving frequencies from $\omega = 0.2$ to 1.6 and amplitude from $F = 0$ and 2.0. The transitions include hysteresis, symmetry breaking (SB), PD, crisis and intermittency. The Feigenbaum and intermittency routes to chaos are observed at, respectively, the right- and left-hand sides of the crossing point with frequency $\omega_C = 0.714$. With suitable choice of initial conditions (or properly chosen scanning amplitude and frequency), the destructive boundary crisis due to the unstable orbit of hysteresis can also be observed with frequency ω less than

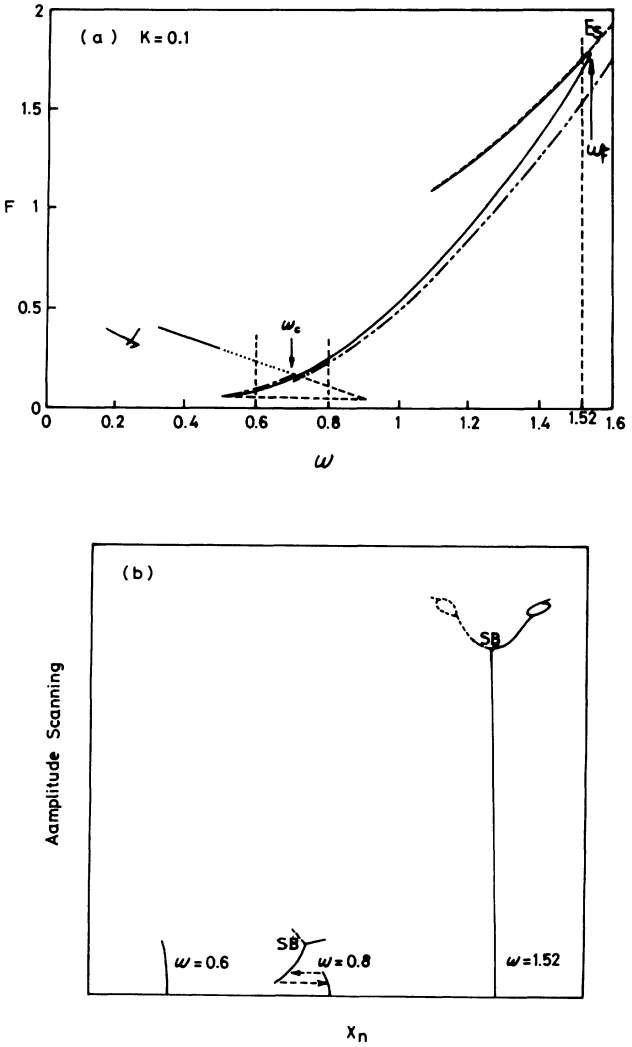

FIG. 5. (a) The state diagram of the symmetrical one-well Duffing oscillator with controlled parameters $k = 0.2$, $\alpha = 1$, and $\gamma = -1$. Curve (——·——) denotes the threshold of symmetry breaking, the solid line (——) denotes the threshold of period bounding, the dashed line (— — —) denotes the threshold of hysteresis jump, the dotted line (· · · ·) denotes the threshold of intermittency, and the short-dashed–long-dashed line (——··——) denotes the threshold of crisis event. The curve E_s represents the border line of escaping the potential well. (b) Bifurcation diagram for amplitude F scanning with driving frequencies $\omega = 0.6$, 0.8, and 1.52, where the marked S denotes the onset of the symmetry breaking.

ω_C [represented by curves (short-dashed–long-dashed)]. Due to the fact that the potential barrier is finite, the transition sequence will be the Feigenbaum or intermittency routes to chaos followed by escaping the potential barrier. The typical bifurcation diagrams are shown in Fig. 5(b). It seem that the symmetry property of the well can suppress the occurrence of the bifurcations including the type-III intermittency and subcritical period doubling. The curve of PD folds back with folding frequency ω_F near 1.54. With the driving frequency higher than the folding frequency ω_F, only the simple period-1 solutions are obtainable.

D. For the case of V_4 potential ($\alpha=1$ and $\beta=1$)

The potential is symmetrical and is infinitely bounded as $|x|\rightarrow\infty$. The state diagram is shown in Fig. 6(a). The shapes of the transition boundaries are no longer like the swallow tail and can be classified into two groups with characteristic shapes associated with odd and even resonances. In the group of odd resonance the shape appears as a horn [24] and only the hysteresis jump is observed without the occurrence of any period doubling. Whereas for the group of even resonance the transition with symmetry breaking is first observed, then hysteresis and period doubling are observed as shown in Fig. 6(b) with $\omega=1.2$. The boundaries of the two groups intersect at the higher excitation amplitudes. It is interesting to note that the shape of thresholds of symmetry breaking is similar to the head of a dolphin with a bump at the upper thresholds. It gives rise to a repeated sequence of SB and reverse SB (RSB) in an amplitude scanning, for example, at frequency $\omega=0.9$ in the region of the bump. The bifurcation diagram is shown in Fig. 6(b). This behavior can be attributed to the coupling of higher-order harmonics.

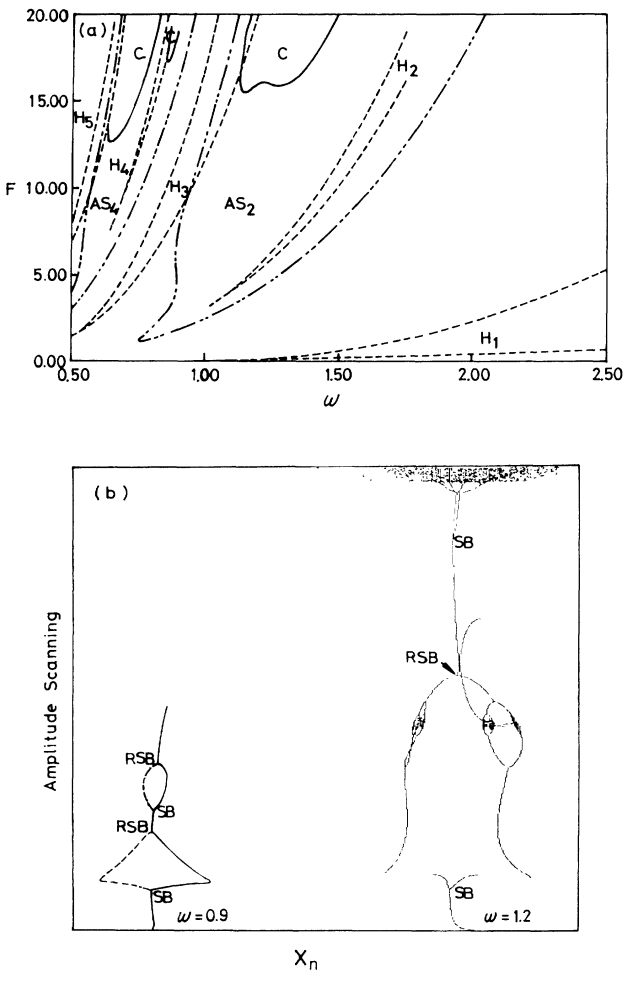

FIG. 6. (a) The state diagram of the infinitely bound symmetrical one-well Duffing oscillator with controlled parameters $k=0.1$, $\alpha=1$, and $\gamma=1$. Curves H_n's (— — —) denote the thresholds of hysteresis jump, curves SB_n's (——·——) denote the thresholds of symmetry breaking, and curves C(——) denote the onset of the first period doubling. (b) The bifurcation diagrams at $\omega=0.9$ and 1.2. The dashed line (— — —) corresponding to the other state is obtained with different initial condition.

III. MATHEMATICAL ANALYSIS

In order to understand the mechanism behind the bifurcations described above, we apply the Floquet theory and the harmonic balance method to analyze the transitions. The approach is briefly described as follows. Based on the numerical results, first, we assume that the differential equation (1) has a stable periodic solution x_0 satisfying $x_0(t+T)=x_0(t)$, where T is the period of external force. In general, one or two dominant modes are selected. Then, a small perturbation δ is added to x_0 to test the stability. Substituting $x=x_0+\delta$ into Eq. (1) and taking the potential into account, we obtain a linearized equation as

$$\frac{d^2\delta}{d\tau^2}+\kappa\frac{d\delta}{d\tau}+\left[+\sum_n Q_n\cos(n\tau+\psi_n)\right]\delta=0\ , \qquad (5)$$

where n is integral, τ is the normalized time, and the coefficients κ, P, Q_n, and ψ_n are all functions of k, F, ω, α, β, γ, and the amplitude of x_0. Equation (5) is referred to as the Hill equation [25]. According to the Floquet theory, the solution $\delta(\tau)$ satisfies $\delta(\tau+T')=\mu\delta(\tau)$, where μ is a Floquet multiplier and T' the least period common to the coefficients in Eq. (5). The instability boundaries in the P-Q plane are the curves on which the Floquet multiplier μ is equal to ±1.

In the meantime, P and Q are functions of the amplitude of x_0 as well as driving force. Thus a locus in the P-Q plane is obtained in amplitude scanning. The occurrence of transition can be predicted when the locus intersects with the instability boundaries with $\mu=\pm1$. And then the type of transition can be characterized from the polarity of the Floquet multiplier. This straightforward method has the advantage of predicting the transitions by inspecting the geometry of the instability boundaries. Moreover, the forward and reverse bifurcations can be figured out as well. In what follows the properties of the various types of bifurcations in each potential well by means of this method will be discussed.

A. For the case of the asymmetrical potential V_1

The equation of motion can be described as

$$\ddot{x}+k\dot{x}+\alpha x+\beta x^2=F\sin(\omega t)\ . \tag{6}$$

From the Fourier spectrum of the numerical simulation, the solution in the period-1 region can be written as

$$x_0(t)=C+A\sin(\omega t+\theta_1)\ , \tag{7}$$

where C, A, and θ_1 are constants to be determined [see Appendix A, Eqs. (A1)–(A3)]. To test how the transition occurs, a small perturbation δ is added to the periodic solution $x_0(t)$. After some algebraic manipulations, the linearized equation with the periodic coefficient for $\delta(\tau)$ is obtained as

$$\frac{d^2\delta}{d\tau^2}+\kappa\frac{d\delta}{d\tau}+[P+Q_1\cos(\tau+\psi_1)]\delta=0\ , \tag{8}$$

where $\kappa=k/\omega$, $\tau=\omega t+\theta_1+\pi/2$, $P=(\alpha+2\beta C)/\omega^2$, $\psi_1=0$, and $Q_1=-2\beta A/\omega^2$. In Eq. (8) two possibilities of instability arise. One is with Floquet multiplier $\mu=+1$, and the other is with $\mu=-1$. We now investigate in detail these two cases.

For $\mu=+1$, the solution of $\delta(\tau)$ has 2π period and can be approximated as

$$\delta(\tau)=\delta_0+\delta_1\cos(\tau+\phi_1)\ , \tag{9}$$

where δ_0, δ_1, and ϕ_1 are constants. The solution δ has the same period as x_0 and corresponds to an SN bifurcation. In experiment, it accounts for the hysteresis jump. The condition for a nontrivial solution is

$$Q^2=2P(P-1)+\frac{2P\kappa^2}{P-1}\ . \tag{10}$$

For $\mu=-1$, the solution $\delta(\tau)$ has a period 4π and can be approximated as

$$\delta(\tau)=\delta_2\cos\left[\frac{\tau}{2}+\phi_2\right]+\delta_3\cos\left[\frac{3\tau}{2}+\phi_3\right]\ . \tag{11}$$

The least frequency of solution δ is half of that of excitation. It corresponds to PD. The condition for the existence of a nontrivial solution is

$$Q^2=\left[2\left[P-\frac{1}{4}\right]+\frac{2(9-4P)Q^2}{(9-4P)^2+36\kappa^2}\right]^2+\left[\kappa+\frac{12\kappa Q^2}{(9-4P)^2+36\kappa^2}\right]^2\ . \tag{12}$$

The sequences of transition can be predicted by examining the interception points of locus and instability boundaries of Eq. (10) and Eq. (12), which are detailed in Figs. 7(a) and 7(b).

From the previous numerical experiment, we see that the PD bifurcation can be either supercritical or subcritical, depending on the driving frequency. In order to elucidate this behavior of the subcritical PD occurring at the subharmonic resonant region, the solution $x_0(t)$ is modified to

$$x(t)=C+A\sin(\omega t+\theta_1)+D\sin(\tfrac{1}{2}\omega t+\theta_2)\ , \tag{13}$$

where D and θ_2 are, respectively, the amplitude and phase of the subharmonic term. The relations among C, A, D, θ_1, θ_2, and F are expressed in Appendix A, Eqs. (A4)–(A8). The bifurcation feature in amplitude scanning can be easily elucidated by examining the relation between driving amplitude F and subharmonic amplitude D. From Eqs. (A4)–(A8), a typical curve of F as a function of D at $\omega=1.8$ is extracted and shown in Fig. 7(c). It illustrates that the existence of hysteresis occurs in the region with $F_u(=4.115)>F>F_d(=2.308)$. In addition, two more features in Fig. 7(c) are discussed subsequently. At first, the subharmonic is not generated until F reaches a threshold value F_u. When F is decreased from a value above F_u, the subharmonic signal D will jump abruptly to zero at $F=F_d$. This feature, in general, accounts for the observation of the occurrence of the hysteresis loop in the case of the subcritical PD bifurcation.

By examining geometrically the functional relationship between the driving force F and the subharmonic amplitude D at the bifurcation point, we see that the sign of the slope $\partial F/\partial D$ at $D=0$, obtainable from Eqs. (A4)–(A8), can be applied to differentiate the types of the PD bifurcation. For the supercritical type, from the functional relation of D versus F, we see that the amplitude D increases monotonically, and a single stable solution exists after the onset of bifurcation, and the slope $\partial F/\partial D$ is positive thereafter; whereas for the subcritical type, the functional relation of D versus F indicates that there exists an unstable state whose slope is less than zero, and a jump occurs immediately at the onset point F_u. It thus turns out that the criterion for differentiating the subcritical and the supercritical PD bifurcations is the sign of the slope $\partial F/\partial D=0$ at $D=0$. Figure 7(d) shows the slope as a function of frequency ω. Note that the type of PD bifurcation is changed at the two critical frequencies $\omega_{s1}(=1.419)$ and $\omega_{s2}(=1.985)$. In other words, the thresholds of supercritical and subcritical PD can be predicted also. The calculated results are in quite good agreement with the state diagram of the numerical simulation as shown in Fig. 7(e).

B. For the case of potential V_2

The equation of motion can be described as

$$\ddot{x}+k\dot{x}+\alpha x+\gamma x^3=F\sin(\omega t)\ . \tag{14}$$

Because the local well is asymmetrical the solution in the period-1 region can be assumed as

$$x_0(t)=C+A\sin(\omega t+\theta_1)+B\sin(2\omega t+\theta_2)\ , \tag{15}$$

where C, A, B, θ_1, and θ_2 are constants to be determined [see Appendix B, Eqs. (B1)–(B5)]. For the testing of linear stability, the same equation of δ as Eq. (8) is used with coefficients $\kappa=k/\omega$, $\tau=\omega t+\theta_1+\phi$,

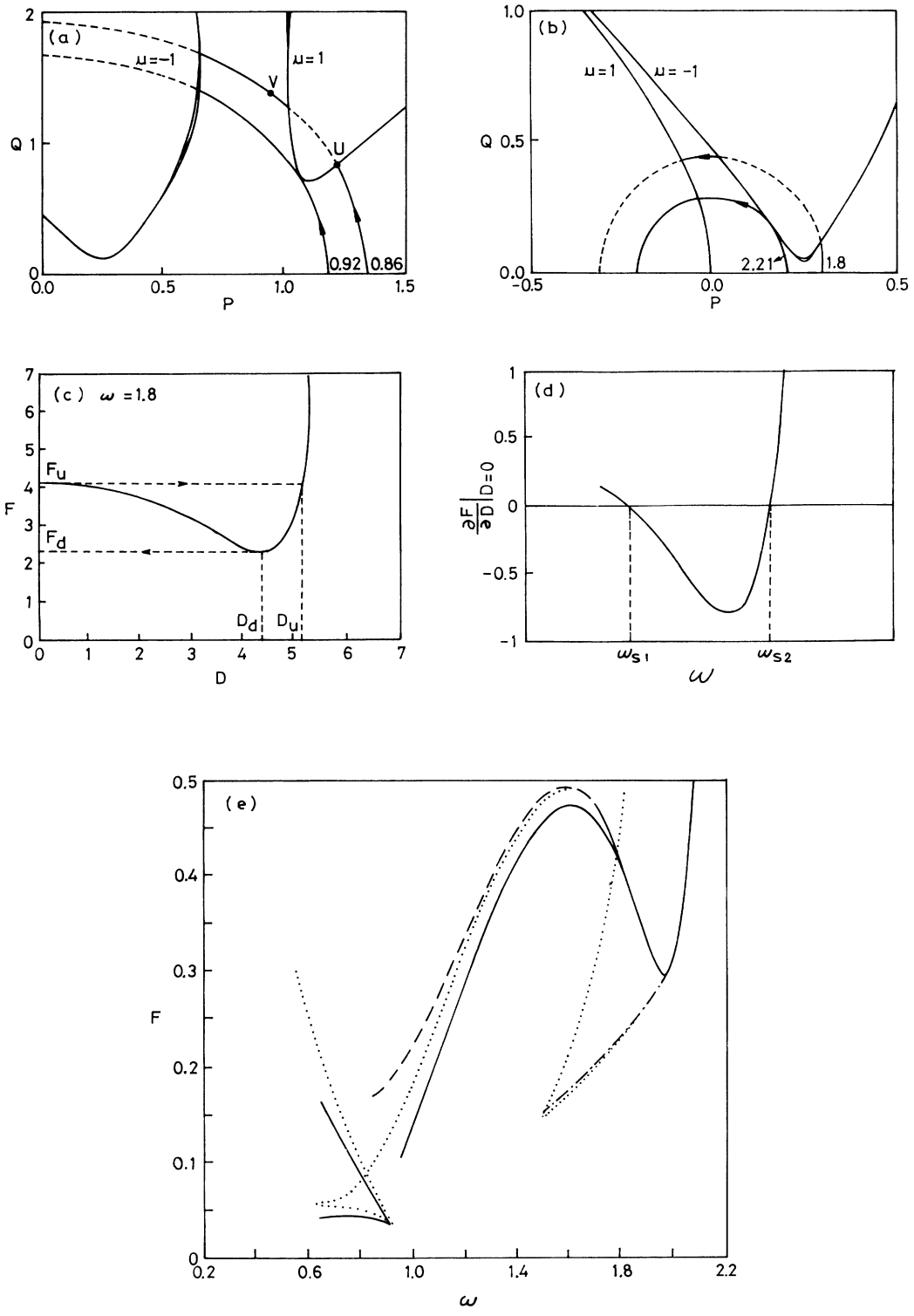

FIG. 7. The stability boundaries with $\mu=\pm 1$ and the locus on the P-Q plane for (a) $\omega=0.92$ and 0.86, (b) $\omega=1.8$ and 2.21. The dashed line denotes the instability part of the locus. The marked points U and V denote the starting and ending point of the hysteresis jump, respectively. (c) The functional relationship between the driven amplitude F and the amplitude of the subharmonic D with $\omega=1.8$. The points F_u and F_d denote the threshold value of the hysteresis upward and downward jump, respectively. (d) The slope $\partial F/\partial D$ at $D=0$ as a function of ω in the subharmonic resonant region. The subcritical bifurcation ($\partial F/\partial D|_{D=0}<0$) is restricted in the range $1.419<\omega<1.985$. (e) Comparison between calculated results and numerical simulation results in the state diagram. The dotted line (· · · ·) denotes numerical results, the solid line (——) denotes the calculation obtained by the single-mode stability boundary, and the dashed line (— — —) denotes the calculation obtained by the two-mode stability boundary.

$$P=[2\alpha+3\gamma(2C^2+A^2+B^2)]/2\omega^2 ,$$

$$Q_1=3\gamma\{[2CA-AB\sin(\theta_2-2\theta_1)]^2 + [AB\cos(\theta_2-2\theta_1)]^2\}^{1/2}/\omega^2 ,$$

$$\phi=\tan^{-1}\left[\frac{AB\cos(\theta_2-2\theta_1)-2CA}{AB\cos(\theta_2-2\theta_1)}\right] .$$

The same as the previous case, the situation with $\mu=+1$ corresponds to SN bifurcation, and $\mu=-1$ corresponds to PD bifurcation. The instability boundaries and locus are detailed in Figs. 8(a) and 8(b) for various ω. For $\omega<1.35$, the locus meets the boundaries first with $\mu=+1$, then with $\mu=-1$. Hence the transition sequence is hysteresis followed by period doubling. The cusp point of hysteresis is at $\omega=1.35$, where the locus is tangential to the instability boundary $\mu=+1$. Only period doubling is observed for $\omega>1.35$. At $\omega=3.25$, the locus is again tangent to the instability boundary so that period doubling disappears for $\omega>3.25$ and the folding frequency ω_F is determined.

In order to further explore the behavior of subcritical PD at the $\omega\approx 3$ region, we examine the solution $x_0(t)$ as expressed in Eq. (13). Here, the amplitude of the second-harmonic term B is very small and thus can be neglected for simplicity. The relations among C, A, D, θ_1, θ_2, and F are listed in Appendix B, Eqs. (B6)–(B10). A typical curve of F as a function of D with $\omega=2.7$ is shown in Fig. 8(c). Obviously, the hysteresis loop occurs with the driving amplitude F between F_u and F_d, which correspond to the dashed line in the state diagram within regime B_I. Also from the criterion of $\partial F/\partial D=0$ at $D=0$, the frequency range of subcritical bifurcation can be found to lie within $\omega_{s1}=2.103$ and $\omega_{s2}=2.817$. And then, the event of the reverse period doubling can be predicted to occur at F_r, where the amplitude of the subharmonic term shrinks to zero, as F is monotonously increased. The analytic results are in very good agreement with the numerical ones presented in Fig. 8(d).

C. For potential V_3

The equation of motion is the same as Eq. (14), where $\alpha>0$ and $\gamma<0$. The solution in the period-1 region can be written as

$$x_0(t)=A\sin(\omega t+\theta_1) , \tag{16}$$

where A and θ_1 are constants to be determined. By the same approach as described before, we obtain the linearized equation Eq. (8) for δ, with coefficients $\kappa=k/2\omega$, $\tau=2(\omega t+\theta_1)$, $P=(\alpha+3\gamma A^2/2)/4\omega^2$, and $Q_1=-3\gamma A^2/8\omega^2$. Unlike before, however, now the Floquet multiplier $\mu=-1$ corresponds to the instability of hysteresis with an extra ωt term generated, whereas $\mu=+1$ corresponds to SB with the emergence of dc and the second harmonic. The instability boundaries are obtained in the P-Q plane as shown in Fig. 9(a). In this figure, for $\omega<0.917$ the locus first meets the hysteresis

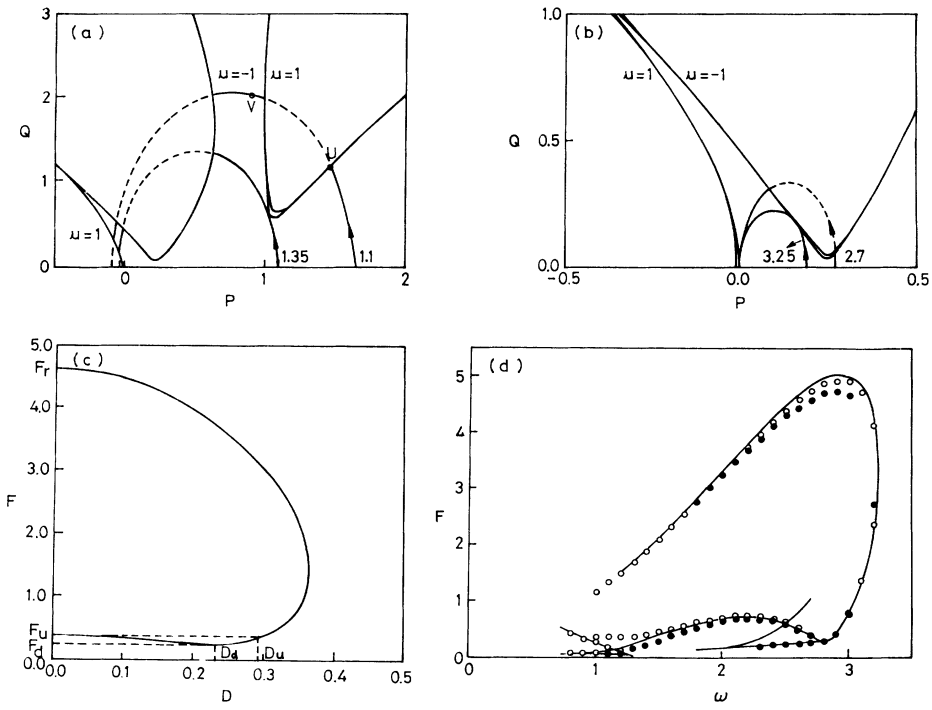

FIG. 8. The instability boundaries with $\mu=\pm 1$ and the loci on the P-Q plane for (a) $\omega=1.1$ and 1.35, (b) $\omega=2.7$ and 3.25. The dashed lines denote the part of the locus within the unstable regions. The starting point and ending point of the hysteresis jump are denoted by U and V, respectively. (c) The functional relationship between the driven amplitude F and the subharmonic amplitude d with $\omega=2.7$. The points F_u and F_d denote the threshold value of the hysteresis up and down jump, respectively. And F_r denotes the threshold value of the reverse period doubling. (d) Comparison of the result of numerical simulation (solid line), the results obtained by the Floquet theory (○) and the results obtained by the harmonic balance method (●) in the state diagram.

boundary with $\mu=-1$ and then the SB one with $\mu=+1$. So the transition sequence is hysteresis first and then follows SB. The cusp point is at $\omega=0.917$. For $\omega>0.917$, only symmetry breaking is observed. Consequently, all the thresholds can be calculated with the aid of the above method. The comparison of the calculated results with the numerical ones is shown in Fig. 9(c).

From the numerical results shown in Fig. 5(b), we know that PD is preceded by symmetry breaking. To find the thresholds of PD, the solution $x_0(t)$ as in Eq. (15) is employed. The transition boundaries of PD are again determined by the criterion $\mu=-1$. The instability boundaries and the locus are shown in Fig. 9(b) for various driving frequencies. The calculated results are also in satisfactory agreement with the numerical ones as shown in Fig. 9(c).

D. For potential V_4

The equation of motion is also the same as Eq. (12), but with $\alpha>0$ and $\gamma>0$. Based on our previous observations, the solution with controlled parameters up to threshold H_3 can be well approximated as

$$x_0(t)=A\sin(\omega t+\theta_1)+B\sin(3\omega t+\theta_3)\ , \tag{17}$$

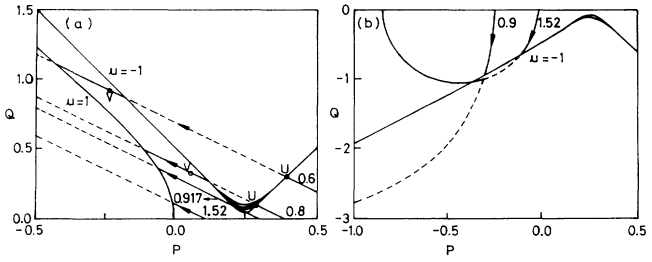

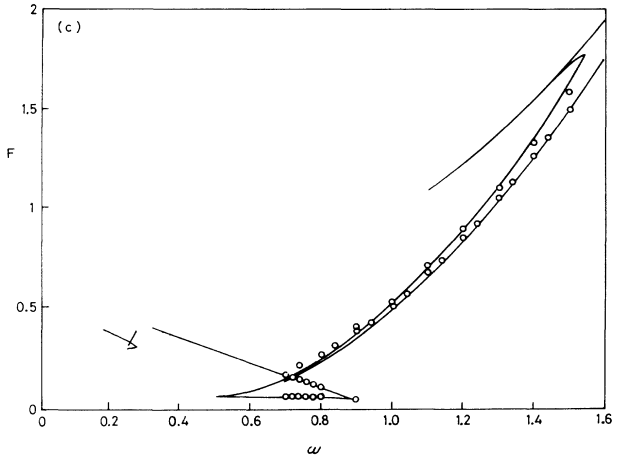

FIG. 9. (a) The instability boundaries with $\mu=\pm1$ and the loci on the P-Q plane for $\omega=0.6$, 0.8, 0.917, and 1.52. (b) The instability boundaries with $\mu=-1$ and the locus on the P-Q plane for $\omega=0.9$ and 1.52. The dashed lines denote the part of the loci within the unstable region. The starting point and ending point of the hysteresis jump are denoted by U and V, respectively. (c) Comparison between the analytic results (○) and numerical simulation results (——) in the state diagram.

where A, B, θ_1, and θ_3 are constants to be determined (see Appendix C). The behavior of hysteresis has been studied [22,23]. Here, we concentrate on analyzing the behavior of SB. To find the instability conditions of SB_2, the linearized equation for δ is obtained as

$$\frac{d^2\delta}{d\tau^2}+\kappa\frac{d\delta}{d\tau}+\delta[P+Q_1\cos(\tau)+Q_2\cos(2\tau+\psi_2)]=0\ , \tag{18}$$

with

$$\kappa=\frac{k}{2\omega}\ ,\quad \tau=2(\omega t+\theta_1)\ ,\quad P=\frac{1}{4\omega^2}[1+\tfrac{3}{2}(A^2+B^2)]\ ,$$

$$Q_1^2=\frac{9}{16\omega^4}[\tfrac{1}{4}A^4-5A^2B^2-4(1-9\omega^2)B^2-3B^4]\ ,$$

$$Q_2^2=\frac{9}{16\omega^4}A^2B^2\ ,$$

$$\psi_2=\eta-\pi-2\tan^{-1}\left[\frac{3AB\sin\eta}{3AB\cos\eta-\frac{3A^2}{2}}\right]\ .$$

According to Floquet theory, the solution δ with Floquet multiplier μ equal to $+1$ is roughly equal to $\delta_0+\delta_2\cos(\tau+\phi_2)$, which corresponds to the emergence of dc and even harmonic 2ω. Here, the higher-order terms are assumed too small to be considered at the onset of symmetry breaking. The instability boundary in the P-Q plane with δ equal to $\delta_0+\delta_2\cos(\tau+\phi_2)$ satisfies

$$Q_1^2=2P\left[P-1+\frac{Q_2\cos\psi_2}{2}\right]+\frac{2P\left[\kappa^2-\frac{(Q_2\sin\psi_2)^2}{4}\right]}{P-1-\frac{Q_2\cos\psi_2}{2}}\ . \tag{19}$$

In the meantime, the locus with the s shape is plotted in the P-Q plane as shown in Fig. 10(a). Curves B_1 and B_2 are the instability boundaries, corresponding to driving amplitudes with $F=1.427$ and 3.961, respectively. The instability boundary is movable, depending on the driving force. The onset points of SB and RSB are graphically determined. As the locus catches up with the instability boundary B_1 at point S, the SB occurs. When the locus intercepts with curve B_2 at point RS, the RSB occurs. According to our analysis, the locus with the driving frequency within the neighborhood of $\omega\approx0.78$ is mostly along the right-hand side of the instability boundary as F is varied. This property leads to the appearance of a bump that resembles a dolphin head, occurring at $\omega\cong0.78$. A comparison of the calculated results is shown in Fig. 10(b). It is quite in agreement with the numerical results. It is believed that if a correction term $\delta_4\cos(2\tau+\phi_4)$ were added to δ, then, the analytic results would be much closer to the numerical ones. From the above analysis we conclude that the curious bump of the upper transition boundary indeed originates from the coupling between fundamental and high-order harmonics.

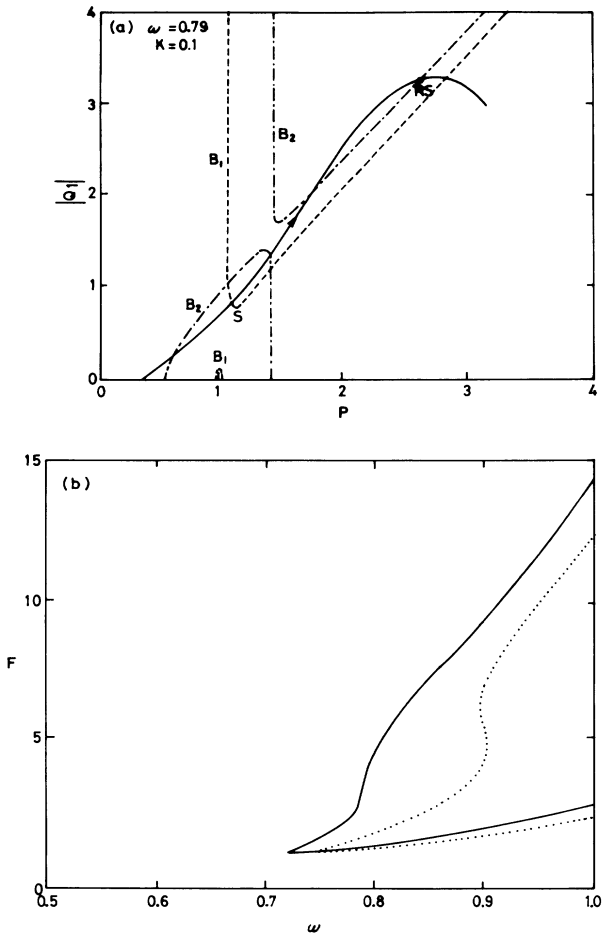

FIG. 10. (a) The curves B_1 and B_2 described by Eq. (19) denote the instability boundaries with Floquet multiplier $\mu=1$. The solid line is the locus with two-mode solution Eq. (18) for $\omega=0.79$. (b) Comparison of the numerical and analytic calculation of SB_2. The dotted line is the numerical result and the solid line is from the analytic calculation.

IV. CONCLUSIONS

In this paper, we have extensively investigated the features of the routes to chaos in Duffing oscillators for four types of potential. Several salient properties are summarized as follows.

(1) The transition boundaries in the state diagram reveal the self-similar behavior in each resonant region. For the cases of the potentials V_1, V_2, and V_3, each possessing an inflection point, the transition boundary line in each resonant region resembles a swallow tail. The swallow-tail-shaped transition boundary includes the following bifurcation types: PD, hysteresis jump, hysteresis induced intermittency and crisis; while, for the V_4 potential, its pattern appears as a horn shape.

(2) The influences of the locally symmetrical potential on the bifurcation are indicated. The type-I intermittency in connection with the supercritical PD bifurcation is observed in all the systems, while the type-III intermittency in connection with the subcritical PD bifurcations is observed in the system with the locally asymmetrical well only.

(3) For the potentials possessing inflection points, the folding back PD can be obtained. From the experimental results, the border line separating the simple periodic solutions from the complicated ones in these systems can be expressed in analytic form. This relation connecting ω_F and k allows us to determine which kind of solution (simple or complicated) can be taken in accordance with the strength of the frequency at a constant damping in the Duffing oscillator. For the case of the symmetrical potential wells (V_2 and sinusoidal) the simple relation $\omega_F=\omega_0[1-(k/k_0)^2]$ is obtained. For the case of the asymmetrical one (V_1), the relation becomes $\omega_F=\omega_0\mathrm{sech}^2(k/k_0)$.

(4) A classical method combining Floquet theory with harmonic balance is presented to calculate the transition boundaries. Here, we get a satisfactory prediction of transition threshold in the numerical simulation, especially for symmetry breaking, the first PD, and the last reverse PD. Actually, the state transitions in a forced system with lower dissipation can be well described from the inherent instability boundaries of the Mathieu equation. Moreover, a crucial condition is also pointed out to differentiate the subcritical PD bifurcation from the supercritical PD bifurcation. The supercritical PD bifurcation can be determined directly by the condition

$$\left.\frac{\partial F}{\partial D}\right|_{D=0}>0 ,$$

where the functional dependence of F on D is obtained from the harmonic balance method, and the value of D can increase monotonically with F near the bifurcation point. While for the subcritical PD bifurcation we have the condition

$$\left.\frac{\partial F}{\partial D}\right|_{D=0}<0 ,$$

and the value of D will jump immediately at the bifurcation point.

ACKNOWLEDGMENTS

The authors would like to thank Mr. Er-Yang Hsu for his reading the manuscript and suggestions. This work was partially supported by the National Science Council of the Republic of China (Taiwan) under Contract No. NSC79-0208-M009-27.

APPENDIX A

Substituting Eq. (7) into the Eq. (6) we obtain the relation among C, A, θ_1, and F as

$$F^2=-\frac{2}{\beta}(\alpha C+\beta C^2)[(k\omega)^2+(\alpha-\omega^2+2\beta C)^2] , \quad \text{(A1)}$$

$$A^2=-\frac{2}{\beta}(\alpha C+\beta C^2) , \quad \text{(A2)}$$

$$\tan(\theta_1)=\frac{k\omega}{\alpha-\omega^2+2\beta C} . \quad \text{(A3)}$$

Substituting Eq. (13) into Eq. (6), we obtain

$$A^2=\frac{1}{4\beta^2}[(k\omega)^2+(2\alpha+4\beta C-\tfrac{1}{2}\omega^2)^2] , \tag{A4}$$

$$D^2=-\frac{2\alpha C}{\beta}-2C^2-A^2 , \tag{A5}$$

$$F^2=\left[-\omega^2 A+\alpha A+2\beta C A+\frac{D^2}{2A}(\tfrac{1}{4}\omega^2-\alpha-2\beta C)\right]^2 + \left[k\omega A+\frac{D^2 k\omega}{4A}\right]^2 , \tag{A6}$$

$$\tan(\theta_1-2\theta_2)=\frac{-\omega^2+4\alpha+8\beta C}{-2k\omega} , \tag{A7}$$

$$\tan(\theta_1)=\frac{4k\omega A^2+k\omega D^2}{-4\omega^2 A^2+4\alpha A+8\beta C A^2+D^2(\omega^2/2-\alpha-2\beta C)} . \tag{A8}$$

APPENDIX B

Substituting Eq. (15) into Eq. (14), we obtain the relations among C, A, B, θ_1, θ_2, and F as

$$(2m)^2+(4k\omega B)^2=(3\gamma C A^2)^2 , \tag{B1}$$

$$2Cn-mB=0 , \tag{B2}$$

$$(lA-2mB)^2+(k\omega A^2+4k\omega B^2)^2=A^2F^2 , \tag{B3}$$

$$\tan(\theta_2-2\theta_1)=\frac{2m}{4k\omega B} , \tag{B4}$$

$$\tan(\theta_1)=\frac{k\omega A^2+4k\omega B^2}{2mB-lA} , \tag{B5}$$

where

$$l=-\omega^2 A+\alpha A+\gamma(\tfrac{3}{4}A^3+3C^2 A+\tfrac{3}{2}AB^2) ,$$

$$m=-4\omega^2 B+\alpha B+\gamma(\tfrac{3}{4}B^3+3C^2 B+\tfrac{3}{2}A^2 B) ,$$

$$n=\alpha C+\gamma(C^3+\tfrac{3}{2}CA^2+\tfrac{3}{2}CB^2) .$$

Substituting Eq. (13) into Eq. (14), we obtain the relation among C, A, D, θ_1, θ_2, and F as

$$m^2+\left[\frac{k\omega D}{2}\right]^2=9\gamma^2 A^2 D^2 C^2 , \tag{B6}$$

$$4Cn-mD=0 , \tag{B7}$$

$$(2Al-mD)^2+\left[2k\omega A^2+\frac{k\omega D^2}{2}\right]^2=4A^2F^2 , \tag{B8}$$

$$\tan(2\theta_2-\theta_1)=\frac{2m}{k\omega D} , \tag{B9}$$

$$\tan(\theta_1)=\frac{4k\omega A^2+k\omega D^2}{2mD-4Al} , \tag{B10}$$

where

$$l=-\omega^2 A+\alpha A+\gamma(\tfrac{3}{4}A^3+3C^2 A+\tfrac{3}{2}AD^2) ,$$

$$m=-\tfrac{1}{4}\omega^2 D+\alpha D+\gamma(\tfrac{3}{4}D^3+3C^2 D+\tfrac{3}{2}A^2 D) ,$$

$$n=\alpha C+\gamma(C^3+\tfrac{3}{2}CA^2+\tfrac{3}{2}CD^2) .$$

APPENDIX C

Substituting Eq. (17) into Eq. (14), we obtain the relations among A, B, θ_1, θ_3, and F as

$$(1-\omega^2)A+\tfrac{3}{4}A^3-\tfrac{3}{4}A^2 B\cos\eta+\tfrac{3}{2}AB^2=F\cos\theta_1 , \tag{C1}$$

$$-k\omega A+\tfrac{3}{4}A^2 B\sin\eta=F\sin\theta_1 , \tag{C2}$$

$$(1-9\omega^2)B+\tfrac{3}{4}B^3-\tfrac{1}{4}A^3\cos\eta+\tfrac{3}{2}A^2 B=0 , \tag{C3}$$

$$3k\omega B+\tfrac{1}{4}A^3\sin\eta=0 , \tag{C4}$$

where $\eta\equiv\theta_3-3\theta_1$, from which the constants A, θ_1, B, and θ_3 can be determined. For convenience, the relation between F and A,B can be expressed as

$$F^2=[-(1-\omega^2)A+\tfrac{3}{4}A^3-\tfrac{3}{4}A^2 B\cos\eta+\tfrac{3}{2}AB^2]^2 + (\omega k A+\tfrac{3}{4}A^2 B\sin\eta)^2 , \tag{C5}$$

via Eqs. (C1) and (C2).

*Electronic address: 7624804@twnctu01.Bitnet.

[1] E. N. Lorenz, J. Atmos. Sci. **20**, 130 (1963).
[2] J. P. Eckmann, Rev. Mod. Phys. **53**, 643 (1981).
[3] E. Ott, Rev. Mod. Phys. **53**, 655 (1981).
[4] T. S. Parker and L. O. Chua, Proc. IEEE **75** (1987).
[5] H. G. Schuster, *Deterministic Chaos: An Introduction* (Physik-Verlag, Weinheim, 1984).
[6] Fa Ou, Phys. Rev. A **41**, 3021 (1990).
[7] M. J. Feigenbaum, J. Stat. Phys. **19**, 25 (1978).
[8] P. Manneville and Y. Pomeau, Commun. Math. Phys. **74**, 189 (180).
[9] D. Ruelle and F. Takens, Commun. Math. Phys. **20**, 167 (1971).
[10] P. Berge, Y. Pomeau, and C. Vidal, *Order Within Chaos* (Wiley, New York, 1984), Chap. 9, pp. 223–263.
[11] J. M. Thompson and H. B. Stewart, *Nonlinear Dynamics and Chaos: Geometrical Methods for Engineers and Scientists* (Wiley, New York, 1987), Chap. 7, pp. 108–131.
[12] B. Ritchie and C. M. Bowden, Phys. Rev. A **32**, 2293 (1985).
[13] B. A. Huberman and J. P. Crutchfield, Phys. Rev. Lett. **43**, 1743 (1979).
[14] P. Holms, Philos, Trans. R. Soc. London, Ser. A **292**, 419 (1979).
[15] F. T. Arecchi and F. Lisi, Phys. Rev. Lett. **49**, 94 (1982).
[16] C. Hayashi, *Nonlinear Oscillations in Physical Systems* (McGraw-Hill, New York, 1964), Chap. 6.
[17] A. H. Nayfey and D. T. Mook, *Nonlinear Oscillations.*
[18] Y. H. Kao, J. H. Huang, and Y. S. Gou, Phys. Rev. A **35**, 5228 (1987).
[19] C. S. Wang, Y. H. Kao, and Y. S. Gou, Phys. Lett. A (to be published).

[20] Y. H. Kao, J. H. Huang, and Y. S. Gou, Phys. Lett. A **131**, 91 (1988).
[21] J. C. Huang, Y. H. Kao, C. S. Wang, and Y. S. Gou, Phys. Lett. A **136**, 131 (1989).
[22] U. Parlitz and W. Lanterborn, Phys. Lett. A **107**, 351 (1985).
[23] Y. H. Kao, C. S. Wang, and T. H. Yang, J. Sound Vibration (to be published).
[24] Thomas S. Parker and Leon O. Chua, *Practical Numerical Algorithms for Chaotic Systems* (Springer-Verlag, New York, 1989).
[25] D. W. Jordan and P. Smith, *Nonlinear Ordinary Differential Equations* (Clarendon, Oxford, 1977), Chap. 7.

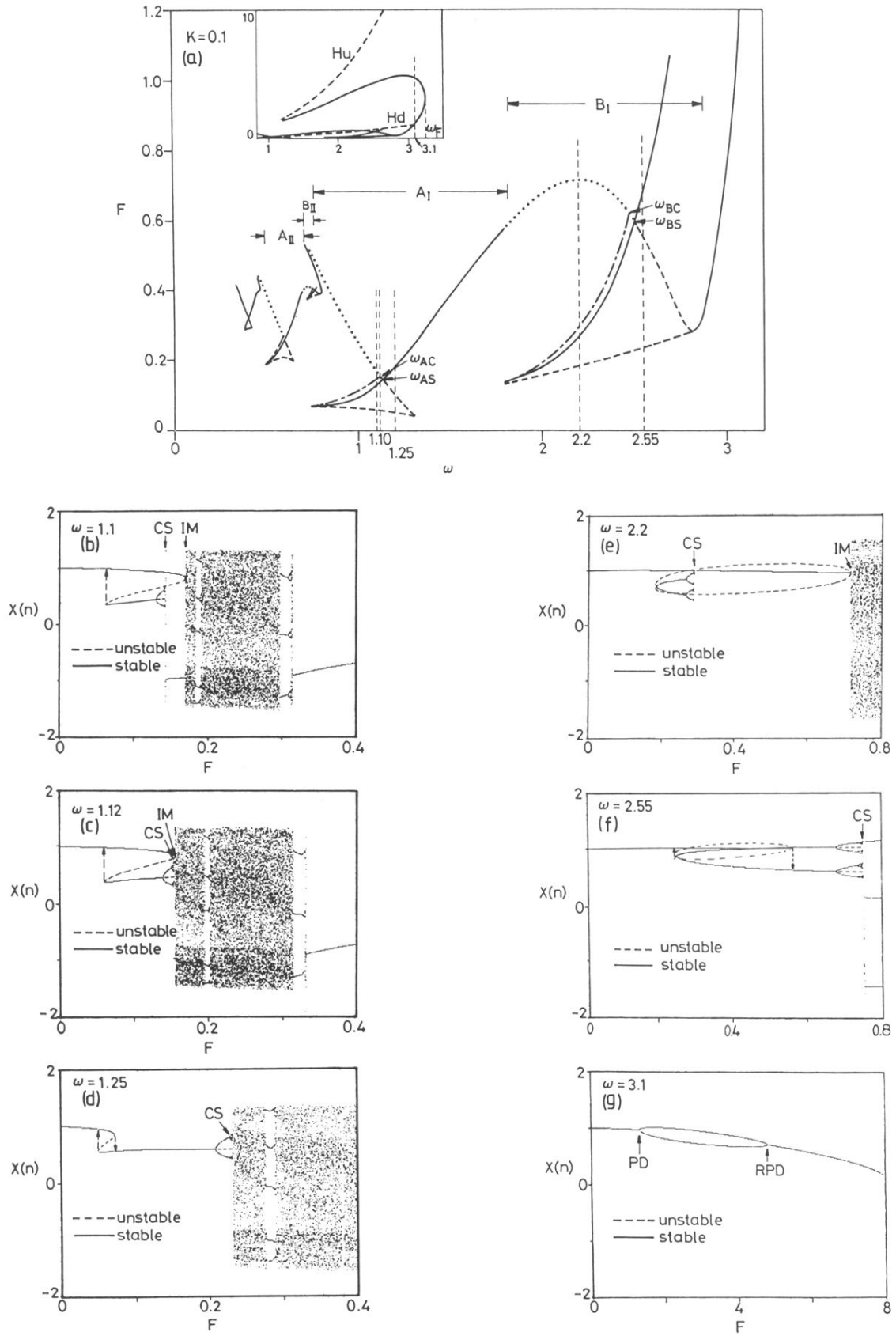

FIG. 3. (a)The state diagram for the two-well potential with controlled parameters $k=0.1$, $\alpha=-1$, and $\gamma=1$. Regions A_1 and B_1 correspond to the primary and subharmonic resonance, respectively. The solid line (——) denotes the threshold of period doubling, the dashed line (— — —) denotes the threshold of hysteresis jump, the dotted line (· · · ·) denotes the threshold of intermittency, and the short-dashed–long-dashed line (—·—·) denotes the threshold of crises event. Bifurcation diagram in amplitude scanning with driven frequency at (b) $\omega=1.1$,(c) $\omega=1.12$ for (d) $\omega=1.25$, (e) $\omega=2.20$, (f) $\omega=2.55$, and (g) $\omega=3.1$.